Int J Adv Manuf Technol (2016) 86:2791–2801
DOI 10.1007/s00170-016-8389-7

ORIGINAL ARTICLE

Groove-center detection in gas metal arc welding using a template-matching method

Xiaojia Wang[1] · **Yonghua Shi**[1] · **Guoqing Yu**[2] · **Bin Liang**[2] · **Yang Li**[1]

Received: 9 July 2015 / Accepted: 13 January 2016 / Published online: 29 January 2016

Abstract To achieve welding automation, the center of the groove needs to be detected accurately during welding. We developed a method based on template-matching to detect the groove center during gas metal arc welding (GMAW). To avoid the negative influence of the strong GMAW arc light, a high-dynamic-range camera was used to capture details of the welding arc, molten pool, and the V-groove simultaneously in a single image. Two image-processing and object-detection algorithms were developed to detect the center of the welding pool and the groove based on template matching. The experimental results of the latter algorithm were more accurate for identifying the position of the groove center. However, interference in the welding process caused the template-matching method to fail under certain conditions. Therefore, the two detection algorithms were combined to improve the detection accuracy. After filtration of the detected welding-pool center, the groove-center detection algorithm based on template matching results in higher accuracy.

Keywords Image processing · Template matching · Seam tracking · High-dynamic-range camera · Gas metal arc welding

1 Introduction

Welding robots are widely used in manufacturing processes; however, most are teaching-playback robots, which cannot self-rectify deviations during the welding process. This means that if the workpieces are changed, the robots must be retaught and reprogrammed. In factories, the weld grooves are not constant in width because of machining tolerance and assembling errors. The groove trajectory also moves during welding because of hot distortion. Therefore, real-time groove tracking is needed to achieve high-quality welds and increase the welding efficiency.

Groove-position detection is the basis of seam tracking. Only accurate extraction of positional information helps to improve groove-tracking accuracy. Owing to its non-contact nature, real-time groove tracking and accuracy, weld-position detection based on visual sensing has been widely studied [1–3]. Kawahara [4] described a highly accurate and widely applicable tracking-control system with a solid-state image sensor that guides a welding torch along a joint line. Smith et al. [5] described a groove tracker to follow the small gap between closed butt plates using a CCD (charge-coupled device) monochrome video camera with a coherent fiber-optic bundle to view the workpiece. Yu et al. [6, 7] studied groove tracking with height variation using vision sensors.

Weld-groove-position detection methods based on visual can be divided into two main categories: active and passive vision. Xu et al. [8] proposed a new scheme of image processing to extract geometrical features of the welding groove from structured light images with arc and splash disturbances. In active-vision methods, laser-structured light is widely used because this simplifies extraction of the groove position. Xu et al. [9] constructed a seam tracking system using a circular laser scanner. However, to avoid strong

---

✉ Yonghua Shi
yhuashi@scut.edu.cn

[1] School of Mechanical and Automotive Engineering, South China University of Technology, Guangzhou, Guangdong 510640, People's Republic of China

[2] Guangzhou Bureau, Navy Armament Department of China, Guangzhou, Guangdong 510300, People's Republic of China

interference of the arc light, the detection area is often in front of the actual welding area. Because of deformation during welding, such methods cannot be used to accurately detect the groove position where the weld is deposited.

By contrast, passive-vision methods provide more detailed information including the shape of the welding arc and groove, and can be used to detect other features, such as the width of the weld pool [10]. Passive vision involves directly capturing both the welding arc and groove in a single image using CCD cameras. Because of the very high intensity of the arc light, the groove appears very dim in the image. Therefore, passive-vision methods are often used in gas tungsten arc welding (GTAW) and pulse welding, in which the welding current is low and therefore the welding arc is not very strong. Shen et al. [11] developed a GTAW robot system and measured in real time the offset of the torch relative to the groove center. Xu et al. [12] analyzed different methods of capturing and processing weld images in real time, and conducted image processing to detect the edges of the groove and pool during GTAW. Because of the stability of the GTAW arc and small image disturbances, algorithms to determine the weld position can be used with high reliability.

For gas metal arc welding (GMAW), Nele et al. presented an automatic groove-tracking system, in which automatic tracking of the welding path and torch positioning is performed using a newly developed image acquisition system [13]. By analyzing the characteristics of robotic GMAW, real-time weld images can be captured clearly by a passive-vision sensor, which enables weld-groove tracking [14]. Because the welding-arc light is much stronger than that used in GTAW and the arc dynamically changes owing to consumption of the electrode, it is difficult to capture a clear image of both the molten pool and the groove during GMAW. Thanks to recently developed high-dynamic-range (HDR) camera technology, it is possible to capture a clear image that contains detailed information of both the molten pool and the groove, and that can be further processed to detect the weld-groove position. In the present study, a HDR camera was used to simultaneously capture details of the welding arc, molten pool, and the V-groove. Detection of the V-groove position from the welding images was studied using a template-matching technique.

2 Experiment setup

The experimental system used consisted of a Panasonic YD-350FR GMAW machine, an ABB 6-joint robot, a shielding gas (CO_2) supply, and an XY motion table equipped with servomotors and fixtures; the experimental setup is shown in Fig. 1. Movement of the workpiece was driven by the XY-axis servomotors. To avoid interference of the high arc-light brightness and to capture images in which the weld groove edge appears near the welding pool, a HDR camera with a 140-dB dynamic range was used. The camera was fixed to the front of the welding gun. The workpiece was driven at a speed of 5 mm/s along the X-axis, and the frame rate of the camera was 25 fps.

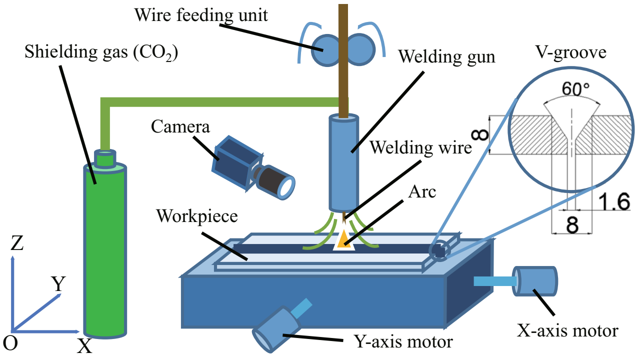

Fig. 1 Schematic diagram of the GMAW experimental system

Different welding parameters can cause varying degrees of interference during image capture. In this study, two different processes with different welding parameters are compared, as detailed in Table 1.

The captured images of two welding processes (i.e., under high and low heat input) with different welding parameters are shown in Fig. 2a, b, respectively. It can be seen that there is larger spatter and a thicker welding fume under high heat input.

3 Detection algorithms for the center of the welding pool and the groove

In real-time groove tracking, the welding torch can be adjusted based on either the center of the welding pool or the center of the groove. Therefore, detection of the positions of both the welding-pool center and groove center is critical.

3.1 Detection of the center of the welding pool

The first step to determine the groove center is to calculate the center of the welding pool because the welding pool is almost symmetric in the V-groove and the center is near the real groove center. As shown in Fig. 3 and outlined below, five image-processing steps were used to identify the center of the welding pool.

Step 1: Selection of the region of interest (ROI) The ROI, as shown in Fig. 3b, is defined as a rectangular area in the image that contains the welding pool region filled in

Table 1 Welding parameters and conditions under high and low heat input

Heat input	Current (A)	Voltage (V)	Shielding gas	Gas flow (L/min)	Welding speed (mm/s)	Welding wire
High	200	24	CO2	large	20	5 flux-cored
Low	150	22	CO2	low	20	5 flux-cored

the V-groove and covers the groove edges. Using the ROI instead of the whole weld image can reduce the number of calculations required during image processing.

Step 2: Median filtering A median-filtering algorithm is used to remove noise in the ROI.

Step 3: Binarization Binarization is used to separate the welding pool region from the background. During welding, the instability of the arc causes the brightness of the image to change, thus making it difficult to apply one specific threshold. Therefore, adaptive threshold-segmentation methods are typically used. Common threshold-segmentation methods include average-gray-value threshold segmentation and Otsus automatic threshold-segmentation method [15]. In this paper, half of the sum of the average gray value and the maximum gray value is selected as the threshold and is calculated using Eq. (1):

$$T = \frac{1}{2}\left(\frac{\sum_{i=1}^{h}\sum_{j=1}^{w} p(i,j)}{h \times w} + \max(p(i,j))\right) \tag{1}$$

where h is the height of the ROI, w is the width of the ROI, $p(i,j)$ is the gray level at position (i,j) in ROI.

A comparison of the image processing results obtained using these three methods is provided in Fig. 4. It is evident that the threshold-selection method developed in this paper is the most effective in imaging the welding pool region.

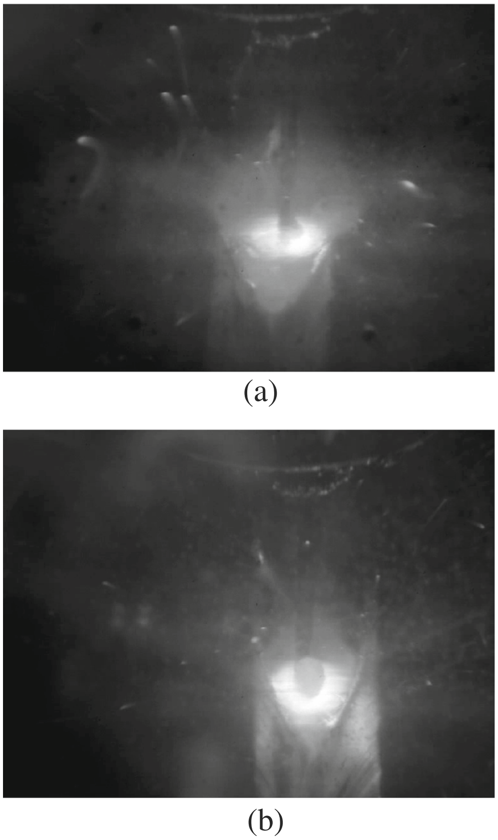
(a)
(b)

Fig. 2 Images captured under **a** high- and **b** low-heat-input welding processes

Step 4: Determination of the largest connected component Spatter is unavoidable during GMAW and produces small white objects after binarization. After obtaining the largest connected component, these small regions are simply removed and the welding pool region is remained. Images processed using this method to obtain the largest connected component under low- and high-spatter

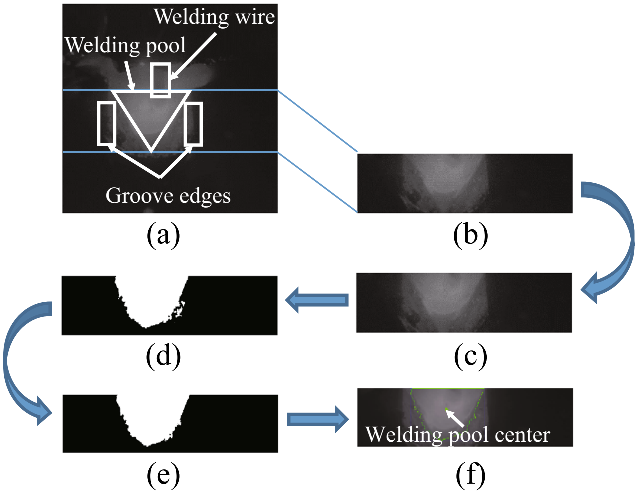

Fig. 3 Image processing to determine the center of the welding pool. **a** Original image. **b** Region of interest. **c** Median filtered image. **d** Binary image. **e** Largest connected component. f Detected center of the welding pool

Fig. 4 Comparison of the image-processing results of the welding pool region for three different threshold-selection methods. **a** Original image. **b** Average-gray-value threshold-selection method. **c** Otsus automatic threshold-selection method. **d** Threshold-selection method developed in the present study

conditions are shown in Fig. 5. The results show that the small white objects from the binary images are no longer present.

Step 5: Calculation of the center of the largest connected component The welding pool in the V-groove is almost symmetrical with its center near the center of the real groove edge. To calculate the center of the welding pool from the image of the largest connected component, we defined the white pixels as and the black pixels as . The center position is calculated with the following equations:

$$\left.\begin{aligned} x_c &= \frac{\sum\limits_{i=1}^{h}\sum\limits_{j=1}^{w} i f(i,j)}{\sum\limits_{i=1}^{h}\sum\limits_{j=1}^{w} f(i,j)} \\ y_c &= \frac{\sum\limits_{i=1}^{h}\sum\limits_{j=1}^{w} j f(i,j)}{\sum\limits_{i=1}^{h}\sum\limits_{j=1}^{w} f(i,j)} \end{aligned}\right\} \tag{2}$$

3.2 Detection of the groove center using template matching

Detection of the welding pool requires accurate computation of the position of the groove edge, which is accomplished using the following four steps (also shown in Fig. 6).

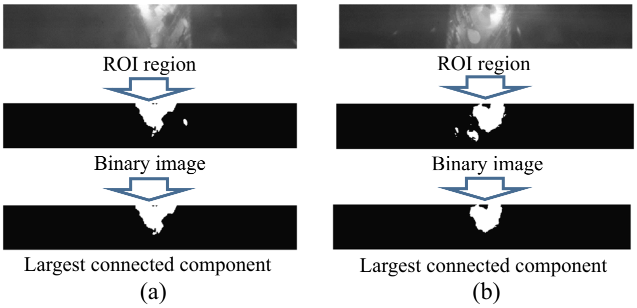

Fig. 5 Comparison of the different processes investigated to obtain the largest connected component under **a** low and **b** high spatter

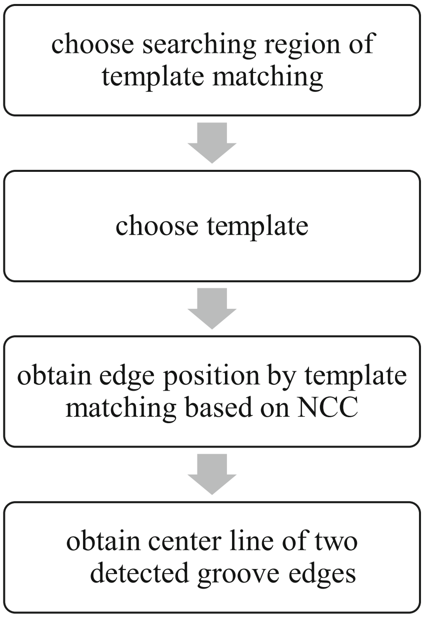

Fig. 6 Flow chart for the detection of the center lines of two groove edges

Step 1: Selection of the search region for template matching The computational cost of the normalized cross correlation (NCC) is very high; thus, it is preferable to reduce the search area while assuring the groove edge is still within this region. It is easier to discern the welding groove edge near the welding pool in the images. Search areas are selected on the left and right sides of the largest connected component, as shown in Fig. 7.

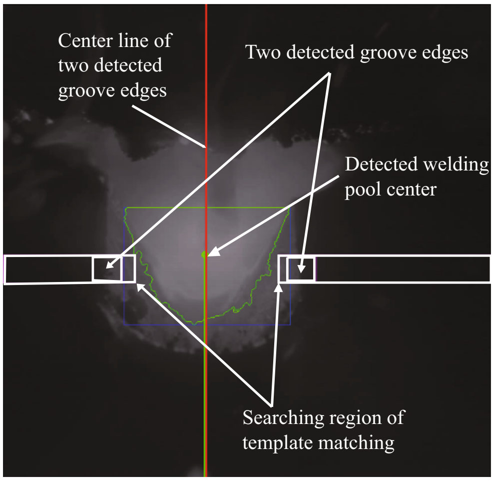

Fig. 7 Image showing the center line of the groove edges

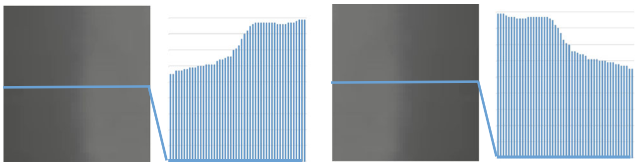

(a) (b)

Fig. 8 Templates used for the left and right groove edges. **a** Template for the left groove edge and its gray-level distribution. **b** Template for the right groove edge and its gray-level distribution

Step 2: Template selection Templates of both the left and right edges are chosen, as shown in Fig. 8. To obtain appropriate templates, welding should be performed. The edge line is chosen in the middle of the template.

Step 3: Template matching based on NCC The template-matching problem can be formulated as follows. Given a source image, I, of size $m \times n$ and a template image, T, of size $M \times N$, the best match of T and I is found with minimum distortion or maximum correlation. NCC is a popular similarity measure and is defined as

$$NCC(x,y) = \frac{\sum_{i=1}^{M}\sum_{j=1}^{N} I(x+i,y+j)T(i,j)}{\sqrt{\sum_{i=1}^{M}\sum_{j=1}^{N} I(x+i,y+j)^2}\sqrt{\sum_{i=1}^{M}\sum_{j=1}^{N} T(i,j)^2}} \tag{3}$$

Where (x, y) is the left-top point of the search window, which is the same size as the template in the source image.

Although template matching with NCC is highly accurate, the traditional NCC method is time-consuming because it computes both the numerator and denominator. In this study, an NCC-based pattern-search algorithm that uses fast Fourier transform (FFT) and integral images was adopted to achieve groove tracking in real time [16]. The NCC equation has the following equivalent transformation:

$$\begin{aligned} NCC(x,y) &= \frac{\sum\limits_{i=1}^{M}\sum\limits_{j=1}^{N}\left[I(x+i,y+j)-I_{aver}^{x,y}\right]\left[T(i,j)-T_{aver}\right]}{\sqrt{\left(\sum\limits_{i=1}^{M}\sum\limits_{j=1}^{N}\left[I(x+i,y+j)-I_{aver}^{x,y}\right]\right)^2}\sqrt{\left(\sum\limits_{i=1}^{M}\sum\limits_{j=1}^{N}\left[T(i,j)-T_{aver}\right]\right)^2}} \\ &= \frac{R_1(x,y)-T_{aver}R_2(x,y)}{\sqrt{R_3(x,y)-\frac{1}{MN}R_2^2(x,y)}\sqrt{\sum\limits_{i=1}^{M}\sum\limits_{j=1}^{N}\left[T(i,j)-T_{aver}\right]^2}} \end{aligned} \tag{4}$$

where T_{aver} is the average gray scale of the template and $I_{aver}^{x,y}$ is the average gray scale of the search window, the formulae of which are shown in Eqs. (5) and (6).

$$T_{aver} = \frac{1}{MN}\sum_{i=1}^{M}\sum_{j=1}^{N} T(i,j) \tag{5}$$

$$I_{aver}^{x,y} = \frac{1}{MN}\sum_{i=1}^{M}\sum_{j=1}^{N} I(x+i,y+j) \tag{6}$$

In Eq. (4), $\sqrt{\sum\limits_{i=1}^{M}\sum\limits_{j=1}^{N}\left[T(i,j)-T_{aver}\right]^2}$ is only associated with the fixed template. Thus, this term can be ignored and we obtain the following equation:

$$NCC'(x,y) = \frac{R_1(x,y)-T_m R_2(x,y)}{\sqrt{R_3(x,y)-\frac{1}{MN}R_2^2(x,y)}} \tag{7}$$

where

$$R_1(x,y) = \sum_{i=1}^{M}\sum_{j=1}^{N} I(x+i,y+j)T(i,j) \tag{8}$$

$$R_2(x,y) = \sum_{i=1}^{M}\sum_{j=1}^{N} I(x+i,y+j) \tag{9}$$

$$R_3(x,y) = \sum_{i=1}^{M}\sum_{j=1}^{N} I^2(x+i,y+j) \tag{10}$$

FFT gives

$$R_1(x,y) = IFFT\left\{I(u,v)\,T^*(u,v)\right\} \tag{11}$$

where $I(u,v)$ is the Fourier transformation of source image I while $T^*(u,v)$ is the conjugate Fourier transformation of template image, T. $IFFT\{\}$ refers to the inverse Fourier transformation.

A complex image, Z, is then constructed as follows:

$$Z(x,y) = I(x,y) + iT(x,y) \tag{12}$$

FFT gives

$$I(u,v) = \left[Z(u,v) + Z^*(M-u,N-v)\right]/2 \tag{13}$$

$$T(u,v) = -i\left[Z(u,v) - Z^*(M-u,N-v)\right]/2 \tag{14}$$

Thus, $R_1(x,y)$ of all search windows can be calculated simultaneously with several simple operations based on FFT.

To accelerate the calculation of R_2 and R_3, the integral image is used. The integral image was introduced by Viola to calculate Haar-like features [17]. For the integral image of the source image I, the gray-scale $ii(x,y)$ is the integration of all gray scales in the top-left corner of the source image:

$$ii\,(x, y) = \sum_{i=1}^{x} \sum_{j=1}^{y} I\,(i, j) \tag{15}$$

For the integral image of I^2, the gray-scale $sii\,(x, y)$ can be calculated as follows:

$$sii\,(x, y) = \sum_{i=1}^{x} \sum_{j=1}^{y} I^2\,(i, j) \tag{16}$$

All $ii\,(x, y)$ and $sii\,(x, y)$ values can be obtained through only one scan of the source image. Then, $R_2\,(x, y)$ and $R_3\,(x, y)$ can be rapidly obtained using the following equations:

$$\begin{aligned}&\sum_{i=1}^{M} \sum_{j=1}^{N} I\,(x+i, y+j)\\ &= ii\,(x+M, y+N) - ii\,(x, y+N)\\ &\quad - ii\,(x+M, y) + ii\,(x, y)\end{aligned} \tag{17}$$

$$\begin{aligned}&\sum_{i=1}^{M} \sum_{j=1}^{N} I^2(x+i, y+j)\\ &= sii\,(x+M, y+N) - sii\,(x, y+N)\\ &\quad - sii\,(x+M, y) + sii\,(x, y)\end{aligned} \tag{18}$$

The NCCs of all search windows are calculated using Eq. (7) to find the maximum NCC; the corresponding position (x, y) is the matched position.

Step 4: Obtaining the center of the edges The center of the edges can be determined after obtaining the positions of the left and right groove edges in the search area.

4 Algorithm accuracy

Using either of the two steps described in the previous section, the center position of the weld groove can be estimated; however, both steps have shortcomings, which lead to instabilities in the detection results and even errors.

4.1 Image calibration

To determine the real lateral distance based on the pixel distance, the captured images should be calibrated. A piece of paper with a planar-checkboard calibration pattern was placed on the workpiece under the welding gun. The point of intersection, P, between the welding wire and the workpiece is shown in Fig. 9a. The size of each lattice of the checkboard was 2 mm x 2 mm. The captured image after distortion is rectified is shown in Fig. 9b, in which p is the projection of P. There is a linear relationship between the real distance of one pixel along the U_0U direction and the V value. As shown in Fig. 9b, in the detection area, when $V = V_1 = 316$, 562 pixels represent 28 mm; when $V = V_2 = 464$, 591 pixels represent 28 mm. Thus, the larger the value of V, the smaller the real distance represented by one pixel.

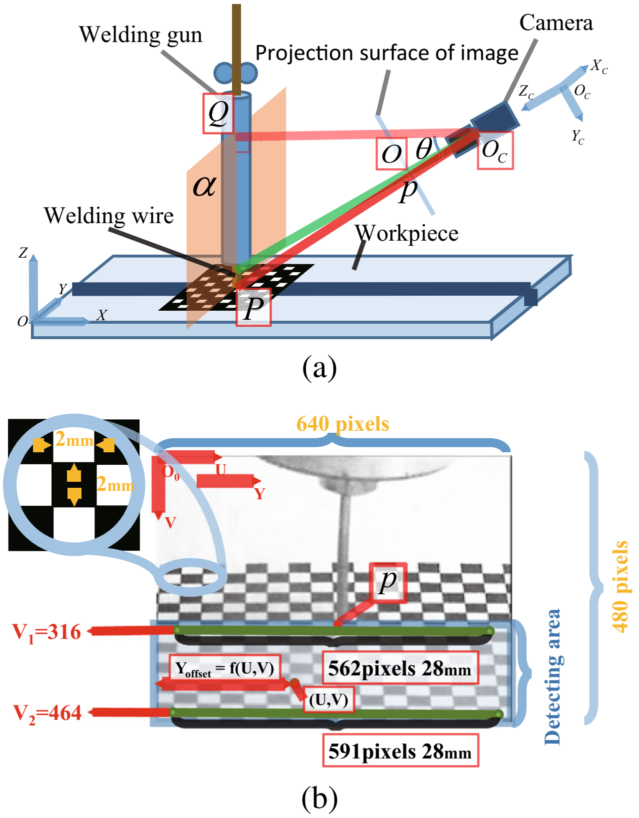

Fig. 9 Image calibration method. **a** Capture method. **b** Captured image after rectification of distortion

Y_{offset} is the real distance from point (U, V) to the O_0V axis and can be calculated as follows:

$$Y_{offset} = U\frac{28}{562 + (591 - 562)\frac{V-316}{464-316}} \tag{19}$$

During welding, the workpiece is prone to deformation and the real center of the groove cannot be calculated in advance. In this study, we used a manually extracted method to obtain the real groove center to assess the accuracy of the algorithms. As shown in Fig. 10a, in the image coordinate system O_0UV, line $V = 358$ and two real groove edges intersect at points A and B. In the coordinate system $OXYZ$, the line is located 5 mm ahead of the welding wire along the OX direction, as shown in Fig. 10b.

The real groove center, C, is the central point of A and B. The Yoffset of C can be calculated as follows:

$$Y_{offset} = U\frac{28}{562 + (591 - 562)\frac{358-316}{464-316}} = 0.05U \tag{20}$$

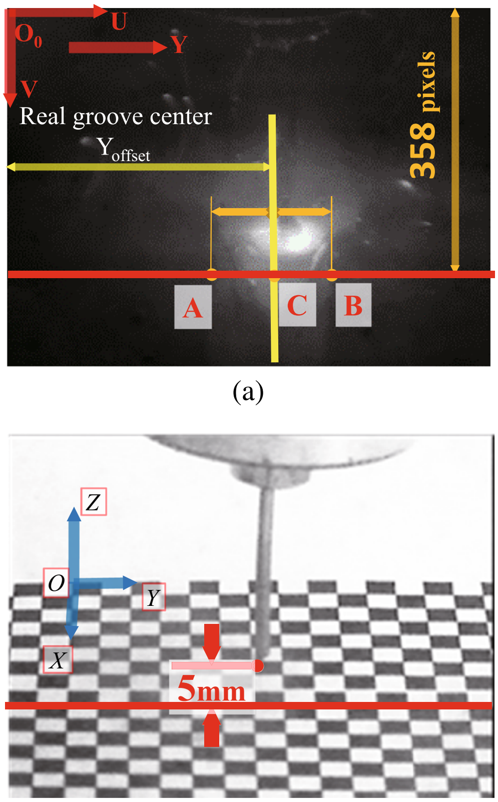

(a)

(b)

Fig. 10 Method of obtaining the real groove center. **a** Measured image coordinate system O_0UV. **b** Position in the coordinate system $OXYZ$

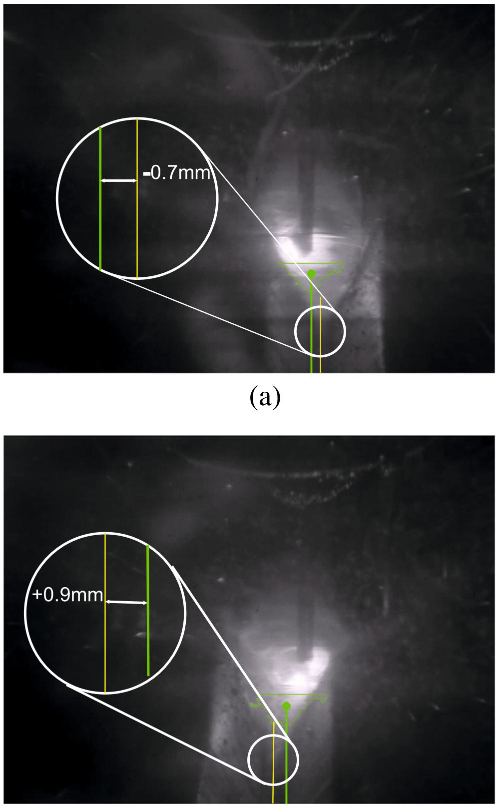

(a)

(b)

Fig. 11 Deviation in the results for the center of the welding pool. **a** Large negative deviation. **b** Large positive deviation

where a value of 0.05 means that one pixel on the line represents 0.05 mm.

4.2 Instability in detecting the center of the welding pool

The results obtained for the center of the welding pool fluctuate around the center position of the real groove within a certain range. During welding, the wire is not always in the center of the groove and the arc is unstable; this causes relatively large fluctuations, as shown in Fig. 11.

4.3 Template-matching error for groove-edge detection

In contrast to the approach described in the previous section, the method of detecting the groove center from two groove edges based on template matching (in the case of an exact match) is more accurate. However, interference during the whole welding process for example, caused by large spatter across the groove edge and a thick welding fume in the template search area results in template-matching error, as shown in Fig. 12.

ROI histograms are shown in Fig. 13 under two different welding conditions. Zone 1 is the workpiece surface next to the groove edges, zone 2 is the groove before the arc, and zone 3 is the welding pool. The ROI image under conditions of high heat input has a lower gray-scale level. Moreover, under these conditions, there is no obvious boundary between zones 1 and 2 in the gray-scale distribution; thus, the edges are not clearly defined. In contrast, under low heat input, there is a larger bright area in the ROI image with more clearly defined edges and the gray-scale distribution between the different zones has a deeper trough. The main reasons for these differences are as follows. In the case of high heat input, the wire melts faster, the degree of melting is higher, and the size of the welding metal and fume is greater. Accordingly, the groove edges become unclear under the thick fume. Moreover, the larger amount of metal filler raises the position of the arc, which makes dark zone 1 brighter and bright zone 2 darker, thereby reducing the gray-scale difference between the two zones. The unclear groove edge in the image leads to template-matching error.

4.4 Improved method

Template-matching errors cause large deviations in the results and therefore must be eliminated. In our method,

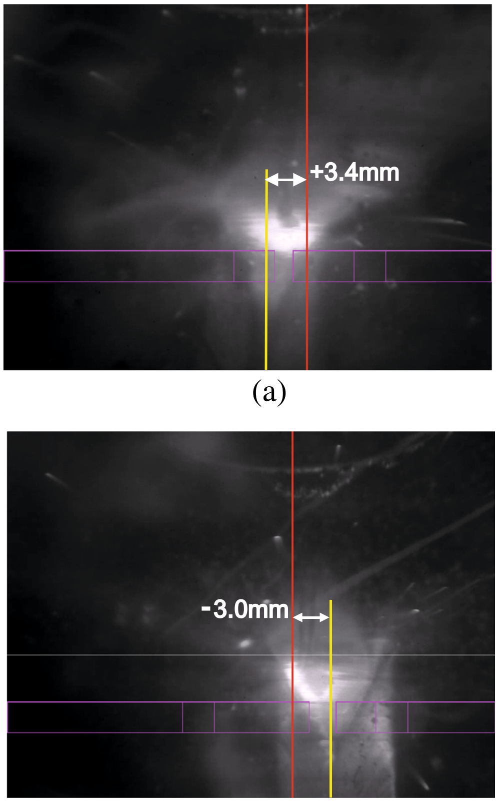

(a)

(b)

Fig. 12 Deviation of the detected central line of two groove edges showing the effect of different types of interference. **a** Interference of spatter. **b** Interference of the welding fume

the fluctuation range of the detected center positions of the welding pool is used as an indicator for template-matching error: if the detected result based on template matching is outside the range of fluctuations of the welding-pool center, the result is ignored.

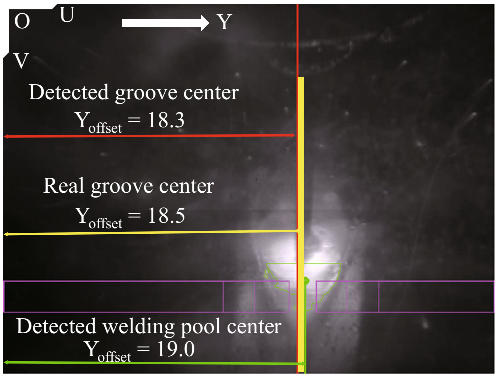

Fig. 14 Annotated image showing the centers of the groove and welding pool

5 Experimental results

Welding experiments were conducted on the platform shown in Fig. 1, and the two welding conditions investigated are shown in Table 1. The centers of the groove and welding pool were calculated using the above-mentioned algorithms from each of the 250 frames recorded, whereas the real groove centers were obtained manually, as shown in Fig. 14. Information was recorded along the Y-direction (in mm) based on the image coordinate OUV in the upper-left corner, as shown as Fig. 14.

Fig. 13 Gray histograms of the ROI under **a** high and **b** low heat input

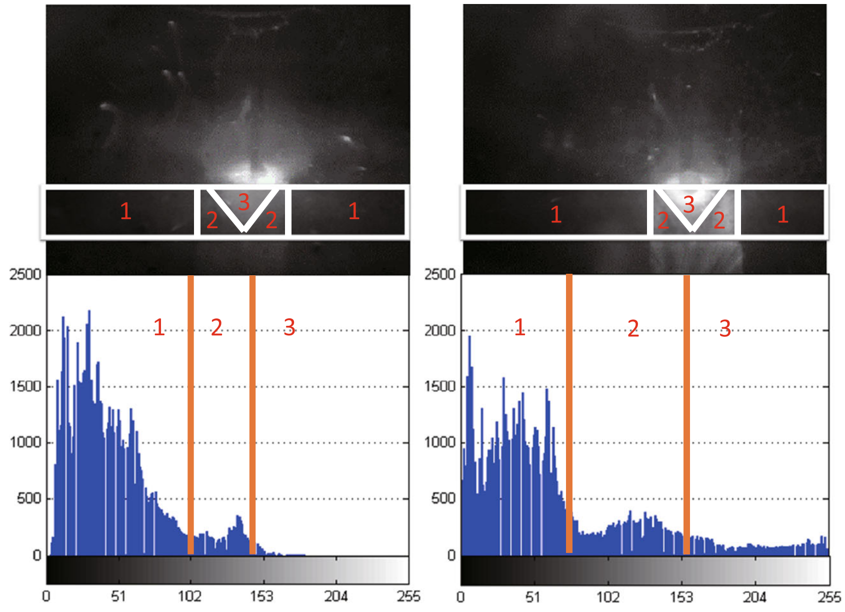

(a)

(b)

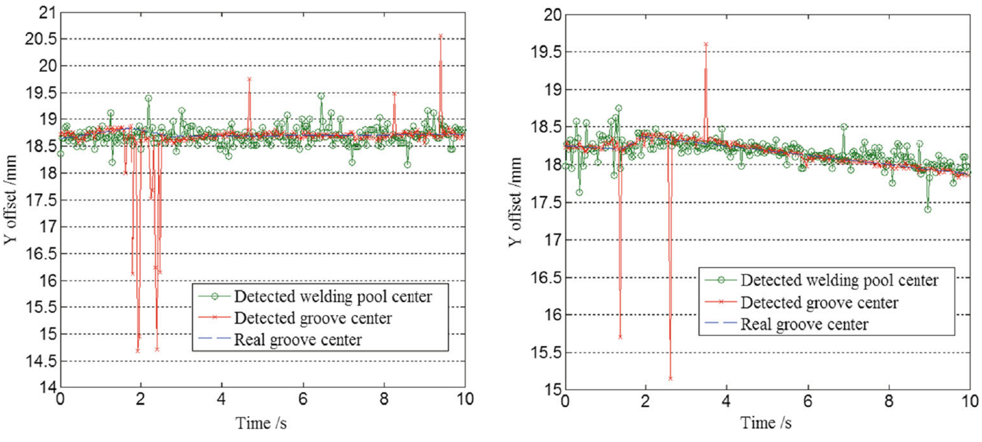

(a) (b)

Fig. 15 *Y*-offset of the results obtained under **a** high and **b** low heat input

The entire welding process includes three phases: arc striking, stable welding, and arc extinguishing. Because of the high current instability in the arc-striking and arc-extinguishing phases, the detected results deviate strongly from the real groove center; these results are disregarded. The results obtained during stable welding are shown as Fig. 15.

Deviations of the two algorithms from the real groove center were calculated, and the results are shown in Fig. 16. Using the template-matching algorithm, it is considered that

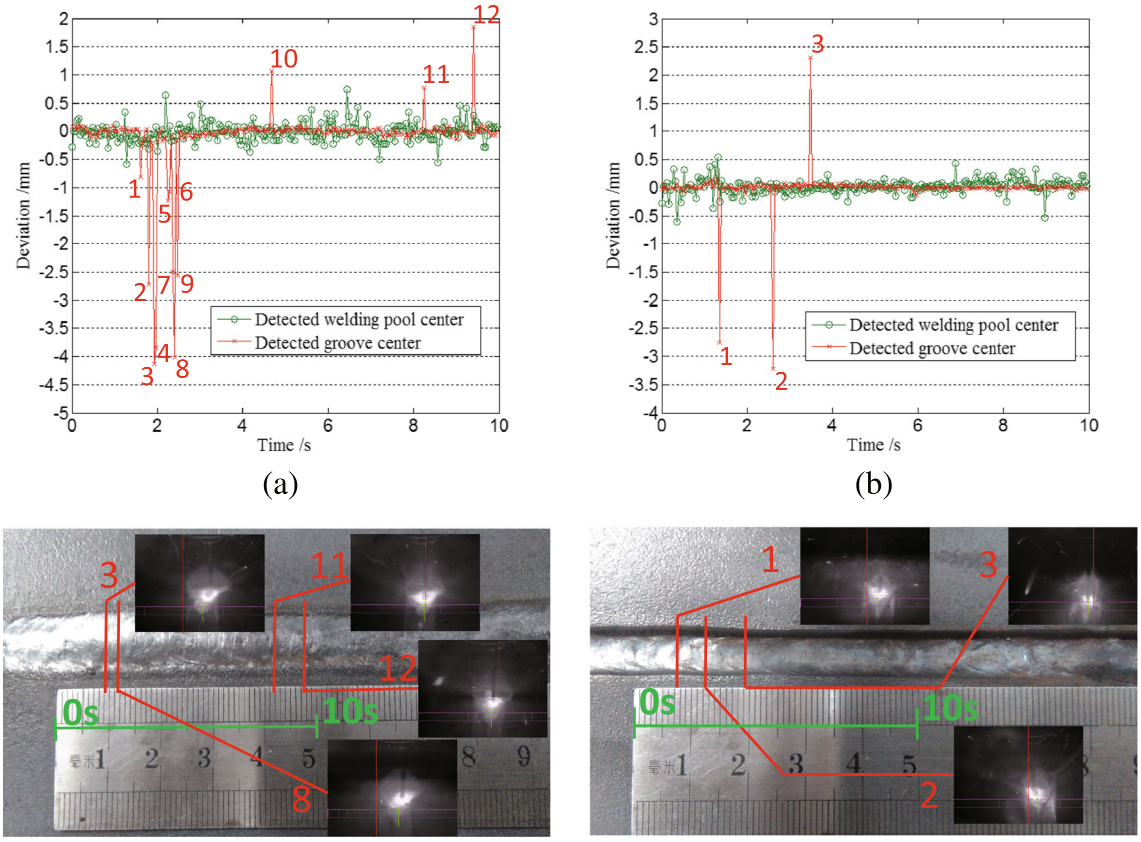

(a) (b)

(c) (d)

Fig. 16 Deviation from the center of the real groove edge under **a** high and **b** low heat input. **c** Top view of the welded workpiece under high heat input. **d** Top view of the welded workpiece under low heat input

Table 2 Accuracy of template matching under high and low heat input

Heat input	Contrast of groove edge	Fume	Splatter	Image number	Number of errors	Accuracy (%)
High	large	thick	large	250	12	95.20
Low	low	thin	low	250	3	98.80

the matching result is erroneous if the absolute value of the deviation between the measured and real groove centers is greater than 0.5 mm. There are 12 matching errors in the case of high heat input and only three in the case of low heat input of the 250 frames captured, as represented in Fig. 16.

The insets in Fig. 16c are marked with numbers 3, 8, 11, and 12, which refer to the matching-error points 3, 8, 11, and 12 in Fig. 16a. For example, inset 3 shows the distance between the red and green lines, which corresponds to a deviation of 4.1 mm (point 3) shown in Fig. 16a. Moreover, the insets in Fig. 16d marked 1, 2, and 3 refer to matching-error points 1, 2, and 3 in Fig. 16b.

The accuracy of template matching was calculated as the number of errors divided by the total number of images. As previously discussed and shown in Table 2, greater spatter and a larger fume are produced under high heat input, which reduces the accuracy of template matching.

There are some large-error data in the results for the groove center based on template matching. If these large-error data are removed, there are only minor variations in the real groove center.

During welding, the template-matching results can be predicted based on the position of the groove center. The weld trajectory within one second typically changes very little and can be approximated as being linear. The results for the groove center can therefore be linearly fitted using the least squares method. This method can be used to filter the interfering data of template matching. Linear fitting parameters are calculated as follows:

$$y_c = a + bt \tag{21}$$

$$a = \frac{\sum_{i=1}^{n} y_{ci} - b \sum_{i=1}^{n} t_i}{n} \tag{22}$$

$$b = \frac{\sum_{i=1}^{n} t_i \sum_{i=1}^{n} y_{ci} - n \sum_{i=1}^{n} t_i y_{ci}}{\left(\sum_{i=1}^{n} t_i\right)^2 - n \sum_{i=1}^{n} {t_i}^2} \tag{23}$$

$$s = \sqrt{\frac{\sum_{i=1}^{n} {t_i}^2 - \frac{\left(\sum_{i=1}^{n} t_i\right)^2}{n}}{n-1}} \tag{24}$$

where y_c is the Y-direction offset of centroid after linear fitting, a is the intercept, b is the slope, s is the standard deviation.

The detected groove center based on template matching must satisfy the following condition:

$$a + bt_i - ks \leq y_{ei} \leq a + bt_i + ks \tag{25}$$

where k is a coefficient that depends on the stability of the arc.

If the obtained results satisfy the condition above, they are used; otherwise, they are considered to be erroneous and are filtered. When the arc is relatively stable, the standard deviation is small. To prevent correct-match data filtering, the coefficient k should increase appropriately in the range from 0.5 to 2. In the filtering process shown in Fig. 17, the predicted data $a + bt_i$ is the reference, $a + bt_i - ks$ is the

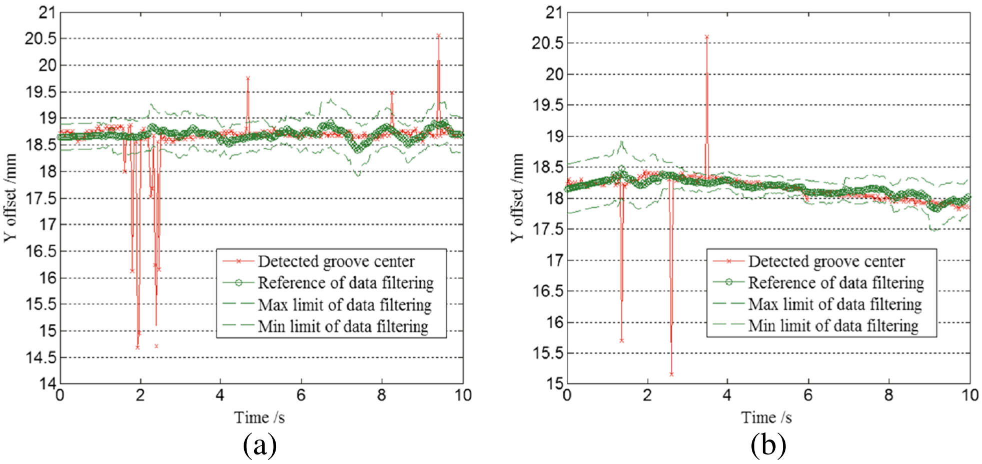

(a) (b)

Fig. 17 Groove center and the filtering process at **a** high heat input and **b** low heat input

Fig. 18 Deviations after filtering at **a** high heat input and **b** low heat input

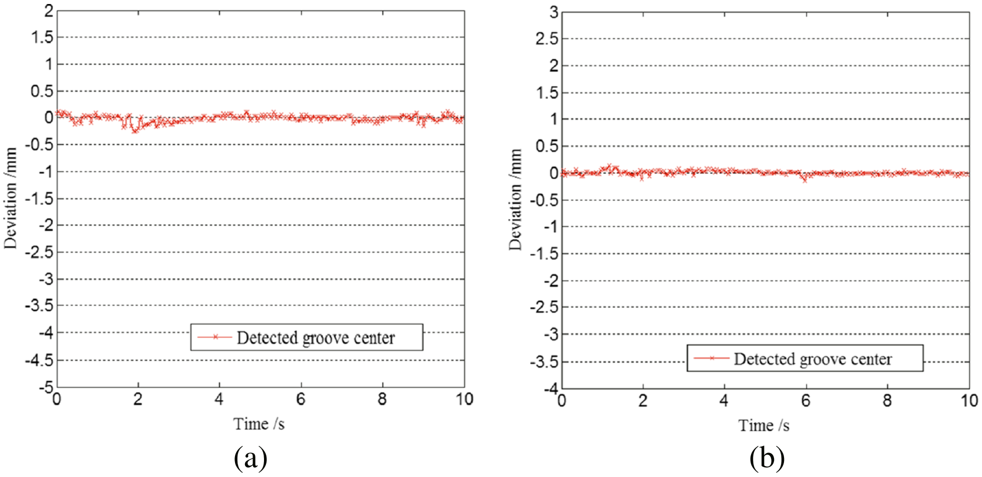

(a) (b)

minimum limit, and $a+bt_i+ks$ is the maximum limit. Deviations after filtering are no greater than 0.3 mm, as shown in Fig. 18.

6 Conclusions

Algorithms to detect the center of the welding pool and groove during GMAW were studied using a template-matching method. The experimental results for the welding-pool center fluctuated around the central position of the groove within a certain range; for groove-center detection, the results were more accurate. However, interference in the welding process can cause failure of the template-matching method. Thus, we proposed an improved method in which the detected result based on template matching is compared with the fluctuation range of the detected welding-pool center. If the template-matching result is outside the fluctuation range of the welding-pool center, it is ignored. The experimental results showed that the groove-center detection algorithm based on template matching provides higher precision after filtration of the linear prediction of the detected welding-pool center.

Acknowledgments This project was supported by the National Natural Science Foundation of China (Grant no. 51374111, 51175185), the Science and Technology Planning Project of Guangdong Province (Grant no. 2015B010919005, 2013B010402005), the Science and Technology Project of Guangzhou City (Grant no. 201510010230), and the Research Project of Navy Armament Department of China.

References

1. Lee SK, Na SJ (2002) A study on automatic seam tracking in pulsed laser edge welding by using a vision sensor without an auxiliary light source. J Manuf Syst 21(4):302–315
2. Chen SB, Zhang Y, Qiu T, Lin T (2003) Robotic welding systems with vision sensing and self-learning neuron control of Arc weld dynamic process. J Intell Robot Syst 36:191–208
3. Ge J, Zhu Z, He D, Chen L (2005) A vision-based algorithm for seam detection in a PAW process for large-diameter stainless steel pipes. Int J Adv Manuf Technol 26(10):1006–1011
4. Kawahara M (1983) Tracking control system using image sensor for arc welding. Automatica 19:357–363
5. Smith JS, Lucas J (1989) A vision-based seam tracker for butt-plate TIG welding. J Phys, E Sci Instrum 22(9):739–744
6. Smith JS, Lucas J (1989) A vision-based seam tracker for butt-plate TIG welding. J Phys E: Sci Inst 22(9):739
7. Yu JY, Na SJ (1997) A study on vision sensors for seam tracking of height-varying weldment, part 1: mathematical model. Mechatronics 7(7):599–612
8. Yu JY, Na SJ (1998) A study on vision sensors for seam tracking of height-varying weldment, part 2: applications. Mechatronics 8(1):21–36
9. Xu P, Xu G, Tang X, Yao S (2007) A visual seam tracking system for robotic arc welding. Int J Adv Manuf Technol 37(1–2):70–75
10. Chen Z, Gao X (2014) Detection of weld pool width using infrared imaging during high-power fiber laser welding of type 304 austenitic stainless steel. Int J Adv Manuf Technol 74:1247–1254
11. Xu D, Jiang Z, Wang L, Tan M (2004) Features extraction for structured light image of welding seam with arc and splash disturbance. In: Proceedings 8th IEEE Control, Automation, Robotics and Vision Conf., vol 3, pp 1559–1563
12. Shen HY, Wu J, Lin T, Chen SB (2008) Arc welding robot system with seam tracking and weld pool control based on passive vision. Int J Adv Manuf Technol 39:669–678
13. Nele L, Sarno E, Keshari A (2013) An image acquisition system for real-time seam tracking. Int J Adv Manuf Technol 69:2099–2110
14. Xu Y, Fang G, Chen S, Zou JJ, Ye Z (2014) Real-time image processing for vision-based weld seam tracking in robotic GMAW. Int J Adv Manuf Technol 73:1413–1425
15. Otsu N (1979) A threshold selection method from gray level histograms. IEEE Trans on SMC 9(1):62–69
16. Yin SF, Wang YC, Cao LC, Jin GF, Ling YS (2010) Fast correlation matching based on fast fourier transform and integral image. Acta Photonica Sin 39(12):2246–2249
17. Viola P, Jones M (2001) Rapid object detection using a boosted cascade of simple features. In: Proceedings IEEE Conference on Computer Vision and Pattern Recognition